18

Massive-Training Artificial Neural Networks (MTANN) in Computer-Aided Detection of Colorectal Polyps and Lung Nodules in CT

Kenji Suzuki, Ph.D.
Department of Radiology, Division of Biological Sciences, The University of Chicago
USA

1. Introduction

Computer-aided diagnosis (CAD) (Giger and Suzuki 2007) has been an active area of study in medical image analysis, because evidence suggests that CAD can help improve the diagnostic performance of radiologists in their image interpretations (Li, Aoyama et al. 2004; Li, Arimura et al. 2005; Dean and Ilvento 2006). Many investigators have participated in and developed CAD schemes for detection/diagnosis of lesions in medical images, such as detection of lung nodules in chest radiographs (Giger, Doi et al. 1988; van Ginneken, ter Haar Romeny et al. 2001; Suzuki, Shiraishi et al. 2005) and in thoracic CT (Armato, Giger et al. 1999; Armato, Li et al. 2002; Suzuki, Armato et al. 2003; Arimura, Katsuragawa et al. 2004), detection of microcalcifications/masses in mammography (Chan, Doi et al. 1987), breast MRI (Gilhuijs, Giger et al. 1998), breast US (Horsch, Giger et al. 2004; Drukker, Giger et al. 2005), and detection of polyps in CT colonography (Yoshida and Nappi 2001; Suzuki, Yoshida et al. 2006; Suzuki, Yoshida et al. 2008). Some advanced CAD schemes employ a filter for enhancement of lesions as a preprocessing step for improving sensitivity and specificity. The filter enhances objects similar to a model employed in the filter; e.g., a blob enhancement filter based on the Hessian matrix enhances sphere-like objects (Frangi, Niessen et al. 1999). Actual lesions, however, often differ from a simple model, e.g., a lung nodule is generally modeled as a solid sphere, but there are nodules of various shapes and inhomogeneous nodules such as a spiculated nodule and a ground-glass opacity. A colorectal polyp is often modeled as a cap structure by using a shape index filter, but a sessile polyp or a flat polyp cannot be characterized well as a cap structure of the shape index. Thus, conventional filters often fail to enhance actual lesions such as lung nodules with ground-glass opacity and sessile/flat polyps.

To address this issue, we developed a supervised filter for enhancement of actual lesions by use of a massive-training artificial neural network (MTANN) (Suzuki, Armato et al. 2003) filter in a CAD scheme. In this chapter, we introduce MTANN-based CAD schemes for detection of lung nodules in CT and for detection of polyps in CT colonography. To summerize, by extension of "neural filters" (Suzuki, Horiba et al. 2002) and "neural edge enhancers" (Suzuki, Horiba et al. 2003; Suzuki, Horiba et al. 2004), which are ANN-based

(Rumelhart, Hinton et al. 1986) supervised nonlinear image-processing techniques, MTANNs (Suzuki, Armato et al. 2003) have been developed for accommodating the task of distinguishing a specific opacity from other opacities in medical images. MTANNs have been applied to the reduction of false positives (FPs) in the computerized detection of lung nodules in low-dose CT (Suzuki, Armato et al. 2003; Arimura, Katsuragawa et al. 2004) and chest radiography (Suzuki, Shiraishi et al. 2005), for distinction between benign and malignant lung nodules in CT (Suzuki, Li et al. 2005), for suppression of ribs in chest radiographs (Suzuki, Abe et al. 2006), and for reduction of FPs in computerized detection of polyps in CT colonography (Suzuki, Yoshida et al. 2006; Suzuki, Yoshida et al. 2008). The MTANN filter is trained with actual lesions in CT images to enhance the actual patterns of the lesions. We evaluated the performance of our CAD schemes incorporating the MTANNs for detection of lung nodules in CT and for detection of polyps in CT colonography.

2. A MTANN Filter for Lesion Enhancement

2.1. An Architecture of an MTANN Filter

To enhance actual lesions in medical images, we developed an MTANN supervised filter. The architecture of an MTANN supervised filter is shown in Fig. 1. An MTANN filter consists of a linear-output regression artificial neural network (LOR-ANN) model (Suzuki, Horiba et al. 2003), which is a regression-type ANN capable of operating on pixel/volel data directly. The MTANN filter is trained with input CT images and the corresponding "teaching" images that contain a map for the "likelihood of being lesions." The pixel values of the input images are linearly scaled such that –1,000 Hounsfield units (HU) corresponds to 0 and 1,000 HU corresponds to 1. The input to the MTANN filter consists of pixel values in a sub-region, R_S, extracted from an input image. The output of the MTANN filter is a continuous scalar value, which is associated with the center pixel in the sub-region, and is represented by

$$O(x,y) = LORANN\{I(x-i,y-j) \mid (i,j) \in R_S\}, \tag{1}$$

where x and y are the coordinate indices, $LORANN(\cdot)$ is the output of the LOR-ANN model, and $I(x,y)$ is a pixel value in the input image. The LOR-ANN employs a linear function, $f_L(u) = a \cdot u + 0.5$, instead of a sigmoid function, $f_S(u) = 1/\{1+\exp(-u)\}$, as the activation function of the output layer unit because the characteristics and performance of an ANN are improved significantly with a linear function when applied to the continuous mapping of values in image processing (Suzuki, Horiba et al. 2003). Note that the activation function in the hidden layers is still a sigmoid function. The input vector can be rewritten as

$$\vec{I}_{x,y} = \{I_1, I_2, \cdots, I_m, \cdots, I_{N_I}\}, \tag{2}$$

where m is an input unit number, and N_I is the number of input units. The output of the n-th unit in the hidden layer is represented by

$$O_n^H = f_S\left\{\sum_{m=1}^{N_I} w_{mn}^H \cdot I_m - w_{0n}^H\right\}, \tag{3}$$

where W^H_{mn} is a weight between the m-th unit in the input layer and the n-th unit in the hidden layer, and W^H_{0n} is an offset of the n-th unit in the hidden layer. The output of the output layer unit is represented by

$$O(x,y) = f_L\left\{\sum_{m=1}^{N_H} w_m^O \cdot O_m^H - w_0^O\right\}, \tag{4}$$

where W^O_m is a weight between the m-th unit in the hidden layer and the unit in the output layer, N_H is the number of units in the hidden layer, and W^O_0 is an offset of the unit in the output layer. For processing of the entire image, the scanning of an input CT image with the MTANN is performed pixel by pixel, as illustrated in Fig. 2(b).

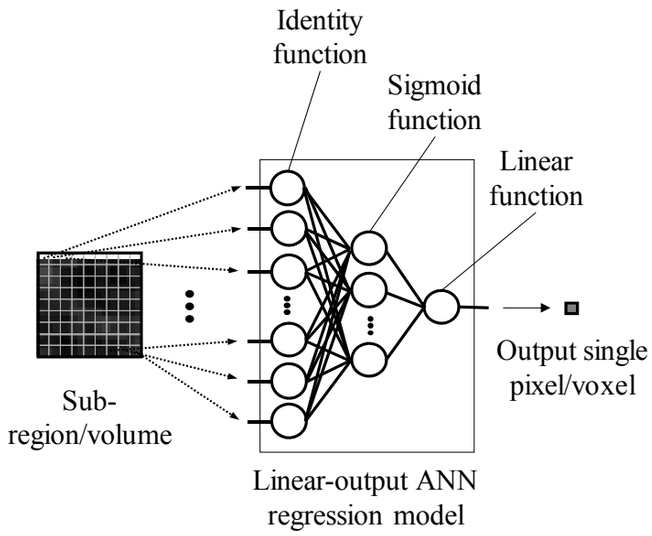

Fig. 1. Architecture of an MTANN supervised filter consisting of a LOR-ANN model with sub-region input and single-pixel output. All pixel values in a sub-region extracted from an input CT image are entered as input to the LOR-ANN. The LOR-ANN outputs a single pixel value for each sub-region, the location of which corresponds to the center pixel in the sub-region. Output pixel value is mapped back to the corresponding pixel in the output image.

2.2. Training of an MTANN Filter

For enhancement of lesions and suppression of non-lesions in CT images, the teaching image $T(x,y)$ contains a map for the "likelihood of being lesions," as illustrated in Fig. 2(a). To create the teaching image, we first segment lesions manually for obtaining a binary image with 1 being lesion pixels and 0 being non-lesion pixels. Then, Gaussian smoothing is applied to the binary image for smoothing down the edges of the segmented lesions, because the likelihood of being lesions should gradually be diminished as the distance from the boundary of the lesion decreases. Note that the ANN was not able to be trained when binary teaching images were used.

The MTANN filter involves training with a large number of pairs of sub-regions and pixels; we call it a massive-sub-region training scheme. For enrichment of the training samples, a training image, R_T, extracted from the input CT image is divided pixel by pixel into a large

number of sub-regions. Note that close sub-regions overlap each other. Single pixels are extracted from the corresponding teaching image as teaching values. The MTANN filter is massively trained by use of each of a large number of input sub-regions together with each of the corresponding teaching single pixels; hence the term "massive-training ANN." The error to be minimized by training of the MTANN filter is given by

$$E = \frac{1}{P}\sum_{c}\sum_{(x,y)\in R_T}\{T_c(x,y) - O_c(x,y)\}^2 \quad , \tag{5}$$

where c is a training case number, O_c is the output of the MTANN for the c-th case, T_c is the teaching value for the MTANN for the c-th case, and P is the number of total training pixels in the training images, R_T. The MTANN filter is trained by a linear-output back-propagation (BP) algorithm where the generalized delta rule (Rumelhart, Hinton et al. 1986) is applied to the LOR-ANN architecture (Suzuki, Horiba et al. 2003). After training, the MTANN filter is expected to output the highest value when a lesion is located at the center of the sub-region of the MTANN filter, a lower value as the distance from the sub-region center increases, and zero when the input sub-region contains a non-lesion.

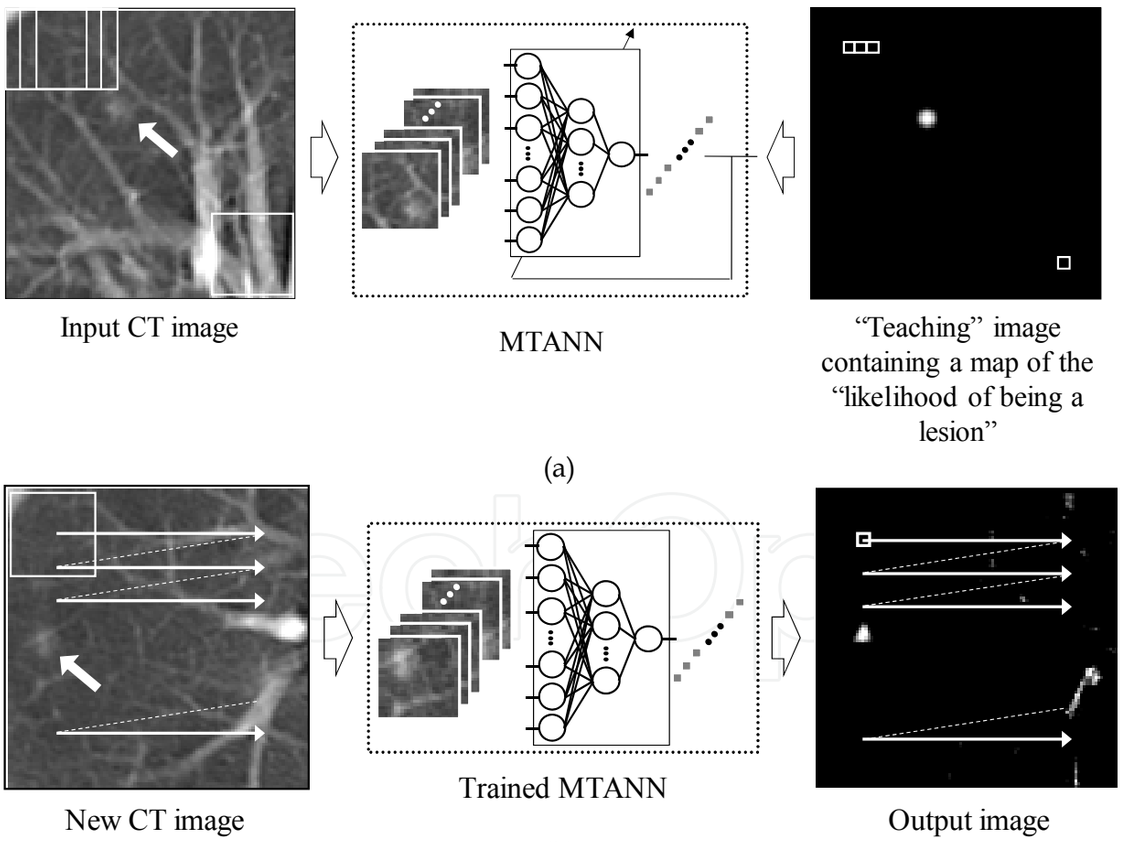

Fig. 2. Training and application of an MTANN filter for enhancement of lesions. (a) Training of an MTANN filter. The input CT image is divided pixel by pixel into a large number of overlapping sub-regions. The corresponding pixels are extracted from the "teaching" image containing a map for the "likelihood of being a lesion." The MTANN filter is trained with

pairs of the input sub-regions and the corresponding teaching pixels. (b) Application of the trained MTANN filter to a new CT image. Scanning with the trained MTANN filter is performed for obtaining pixel values in the entire output image.

3. An MTANN for Classification

3.1. A Training Method of an MTANN for Classification

For distinction between lesions and non-lesions in medical images, the teaching image contains a Gaussian distribution with standard deviation σ_T for a nodule and zero for a non-nodule (i.e., completely dark), as shown in Fig. 3. This distribution represents a map for the "likelihood of being a lesion":

$$T(x,y) = \begin{cases} \dfrac{1}{\sqrt{2\pi}\sigma_T} \exp\left\{-\dfrac{(x^2+y^2)}{2\sigma_T{}^2}\right\} & \textit{for a lesion} \\ 0 & \textit{otherwise.} \end{cases} . \tag{6}$$

To enrich the training samples, a training region, R_T, extracted from the input image is divided pixel by pixel into a large number of overlapping sub-regions. Single pixels are extracted from the corresponding teaching region as teaching values. The MTANN is massively trained by use of each of a large number of the input sub-regions together with each of the corresponding teaching single pixels. After training, the MTANN is expected to output the highest value when a lesion is located at the center of the sub-region of the MTANN, a lower value as the distance from the sub-region center increases, and zero when the input sub-region contains a non-lesion.

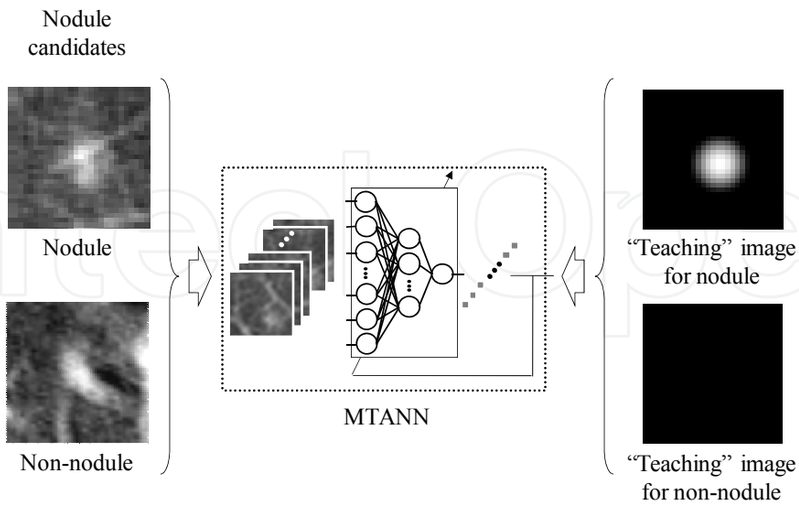

Fig. 3. Architecture and training of an MTANN for classification of candidates into a lesion (e.g., a nodule) or a non-lesion (e.g., a non-nodule). A teaching image for a nodule contains a Gaussian distribution at the center of the image, whereas that for a non-nodule contains zero (i.e., it is completely dark).

3.2. A Scoring Method for Combining Output Pixels

For combining output pixels from a trained MTANN, we developed a scoring method. A score for a given lesion candidate from the trained MTANN is defined as

$$S = \sum_{(x,y)\in R_E} f_G(\sigma; x, y) \times O(x, y) \tag{7}$$

where

$$f_G(\sigma; x, y) = \frac{1}{\sqrt{2\pi}\sigma} \exp\left\{-\frac{(x^2 + y^2)}{2\sigma^2}\right\} \tag{8}$$

is a Gaussian weighting function with standard deviation σ, and with its center corresponding to the center of the region for evaluation, R_E; and $O(x,y)$ is the output region of the n-th trained MTANN, where its center corresponds to the center of R_E. The use of the Gaussian weighting function allows us to combine the responses (outputs) of a trained MTANN as a distribution. A Gaussian function is used for scoring, because the output of a trained MTANN is expected to be similar to the Gaussian distribution used in the teaching region. This score represents the weighted sum of the estimates for the likelihood that the region (lesion candidate) contains a lesion near the center, i.e., a higher score would indicate a lesion, and a lower score would indicate a non-lesion.

3.3. A Mixture of Expert MTANNs

To distinguish lesions from various types of non-lesions (or FPs), we have extended the capability of a single MTANN, and have developed a mixture of expert MTANNs. The architecture of the mixture of expert MTANNs is shown in Fig. 4(a). The mixture of expert MTANNs consists of several MTANNs that are arranged in parallel. Each MTANN is trained independently by use of the same nodules and a different set of non-nodules, as shown in Fig. 4(b). Each MTANN acts as an expert for distinction between lesions (e.g., nodules) and non-lesions (e.g., non-nodules) representing a specific non-lesion type. The scores from the expert MTANNs are combined by use of a mixing ANN such that different types of non-lesions can be distinguished from lesions. The mixing ANN consists of a linear-output multilayer ANN model with a linear-output BP training algorithm (Suzuki, Horiba et al. 2003) for processing of continuous output/teaching values; the activation functions of the units in the input, hidden, and output layers are an identity, a sigmoid, and a linear function, respectively. One unit is employed in the output layer for distinction between a lesion and a non-lesion. The scores of each expert MTANN are used for each input unit in the mixing ANN; thus, the number of input units corresponds to the number of expert MTANNs, N. The scores of each expert MTANN act as the features for distinguishing lesions from a specific type of non-lesion for which the expert MTANN is trained. The output of the mixing ANN for the c-th lesion candidate is represented by

$$M_c = NN\left[\{S_{n,c}\} \mid 1 \le n \le N\right], \tag{9}$$

where $NN(\cdot)$ is the output of the linear-output ANN model, and n is an MTANN number. The teaching values for lesions are assigned the value one, and those for non-lesions are

zero. Training of the mixing ANN may be performed by use of a leave-one-lesion-out cross-validation scheme (Mosier 1951). After training, the mixing ANN is expected to output a higher value for a lesion and a lower value for a non-lesion. Thus, the output can be considered to be a "likelihood of being a lesion." By thresholding the output, a distinction between lesions and non-lesions can be made. The balance between a true-positive rate and an FP rate is determined by the selected threshold value. If the scores of each expert MTANN properly characterize the specific type of non-lesion for which the expert MTANN is trained, the mixing ANN combining several expert MTANNs will be able to distinguish lesions from various types of non-lesions.

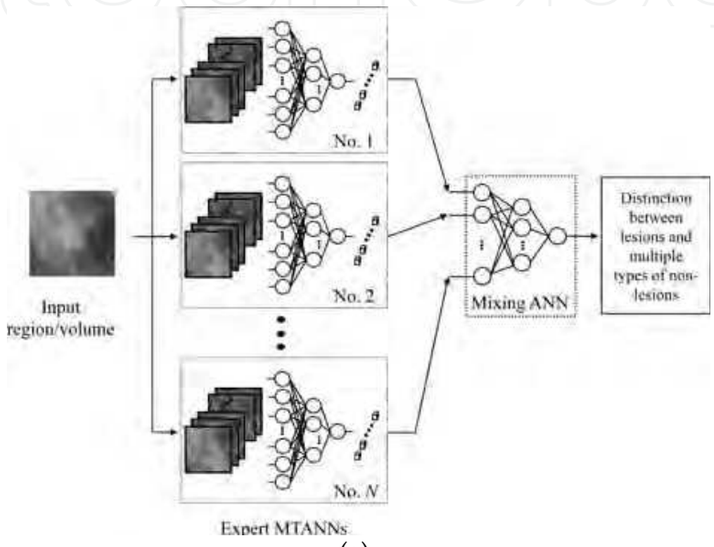

Fig. 4. Architecture (a) and training (b) of a mixture of expert MTANNs for classification of lesion candidates into lesions or multiple types of non-lesions.

4. A CAD Scheme for Detection of Lung Nodules on CT Images

4.1. Lung Cancer Detection in CT

Lung cancer continues to rank as the leading cause of cancer deaths among Americans (American:Cancer:Society 2005; Jemal, Murray et al. 2005); the number of lung cancer deaths each year is greater than the combined number of breast, colon, and prostate cancer deaths. Evidence suggests that early detection of lung cancer may allow more timely therapeutic intervention and thus a more favorable prognosis for the patient (Heelan, Flehinger et al. 1984; Flehinger, Kimmel et al. 1992; Sobue, Suzuki et al. 1992; Miettinen 2000). Therefore, in the 1970s, screening programs for early detection of lung cancer were carried out with chest radiography and cytologic examination of sputum in the United States (Flehinger, Melamed et al. 1984; Fontana, Sanderson et al. 1984; Frost, Ball et al. 1984) and in Europe (Kubik and Polak 1986). As the CT imaging techniques have advanced, screening with low-dose helical CT has been performed for early detection of lung cancer (Kaneko, Eguchi et al. 1996; Sone, Takashima et al. 1998; Henschke, McCauley et al. 1999; Henschke, Naidich et al. 2001; Miettinen and Henschke 2001; Sone, Li et al. 2001; Nawa, Nakagawa et al. 2002; Swensen, Jett et al. 2003) since early 1990.

Because CT is more sensitive than chest radiography in the detection of small non-calcified nodules due to lung carcinoma at an early stage (Sone, Takashima et al. 1998; Miettinen and Henschke 2001), lung cancer screening programs are being conducted in the United States (Henschke, McCauley et al. 1999; Henschke, Naidich et al. 2001; Miettinen and Henschke 2001; Swensen, Jett et al. 2003) and Japan (Kaneko, Eguchi et al. 1996; Sone, Takashima et al. 1998; Sone, Li et al. 2001; Nawa, Nakagawa et al. 2002) with low-dose single-detector CT as the screening modality. Recently, multi-detector-row CT (MDCT) has been used for lung cancer screening. Helical CT and MDCT, however, generate a large number of images that must be read by radiologists. This may lead to "information overload" for radiologists. Furthermore, radiologists may fail to detect some cancers, which are visible in retrospect, during the interpretation of CT images (Gurney 1996; Li, Sone et al. 2002). Therefore, a CAD scheme for detection of lung nodules in CT has been investigated as a tool for lung cancer screening, because the CAD scheme may detect some cancers that are "missed" by radiologists (Li, Sone et al. 2002), and provide quantitative detection results as a "second opinion" to assist radiologists in improving their detection accuracy (Kobayashi, Xu et al. 1996).

4.2. Database of Lung Nodules in CT

To test the performance of a CAD scheme utilizing the MTANN filters, we created a CT database consisting of 69 lung cancers in 69 patients (Li, Sone et al. 2002). The scans used for this study were acquired with a low-dose protocol of 120 kVp, 25 mA or 50 mA, 10-mm collimation, and a 10-mm reconstruction interval at a helical pitch of two. The reconstructed CT images were 512 x 512 pixels in size with a section thickness of 10 mm. The 69 CT scans consisted of 2,052 sections. All cancers were confirmed either by biopsy or surgically.

4.3. Detection of Nodule Candidates

The flowchart of our CAD scheme utilizing the MTANN supervised lesion enhancement filter and the MTANNs for classification is shown in Fig. 5. To limit processing area to the lungs, we segmented the lung regions in a CT image by use of thresholding based on Otsu's

threshold value determination (Otsu 1979). Then, we applied a rolling-ball technique along the outlines of the extracted lung regions to include a nodule attached to the pleura in the segmented lung regions (Armato, Giger et al. 2001).

To enhance lung nodules in CT images, we trained an MTANN filter with 13 lung nodules in a training database and the corresponding "teaching" images that contained maps for the "likelihood of being nodules," as illustrated in Fig. 2(a). To obtain the training regions, R_T, we applied a mathematical morphology opening filter to the manually segmented lung nodules (i.e., binary regions) such that the training regions sufficiently covered nodules and surrounding normal structures (i.e., a 9 times larger area than the nodule region, on average). A three-layer structure was employed for the MTANN filter, because any continuous mapping can be approximated by a three-layer ANN (Funahashi 1989). The number of hidden units was selected to be 20 by use of a method for designing the structure of an ANN (Suzuki, Horiba et al. 2001; Suzuki 2004). The size of the input sub-region, R_S, was 9 by 9 pixels, which was determined experimentally in our previous studies (Suzuki, Armato et al. 2003; Arimura, Katsuragawa et al. 2004; Suzuki and Doi 2005). The slope of the linear function, a, was 0.01. With the parameters above, training of the MTANN filter was performed by 1,000,000 iterations. To test the performance, we applied the trained MTANN filter to the entire lungs. We applied thresholding to the output images of the trained MTANN filter to detect nodule candidates. We compared the results of nodule-candidate detection with and without the MTANN filter.

We applied the trained MTANN filter to original CT images. The result of enhancement of nodules in CT images by the trained MTANN filter is shown in Fig. 6. The MTANN filter enhances the nodule and suppresses most of the normal structures in the CT image. Although some medium-sized vessels and some of the large vessels in the hilum remain in the output image, the nodule with spiculation is enhanced well. We applied thresholding to the output images of the trained MTANN filter. There are a smaller number of candidates in the MTANN-based image, as illustrated in Fig 6(c), whereas there are many nodule candidates in the binary image obtained by use of simple thresholding without the MTANN filter, as shown in Fig. 6(d). Note that the large vessels in the hilum can easily be separated from nodules by use of their area information.

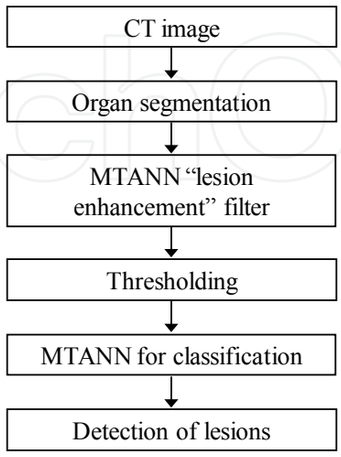

Fig. 5. Flowchart of our CAD scheme utilizing the MTANN supervised lesion enhancement filter and the mixture of expert MTANNs for classification.

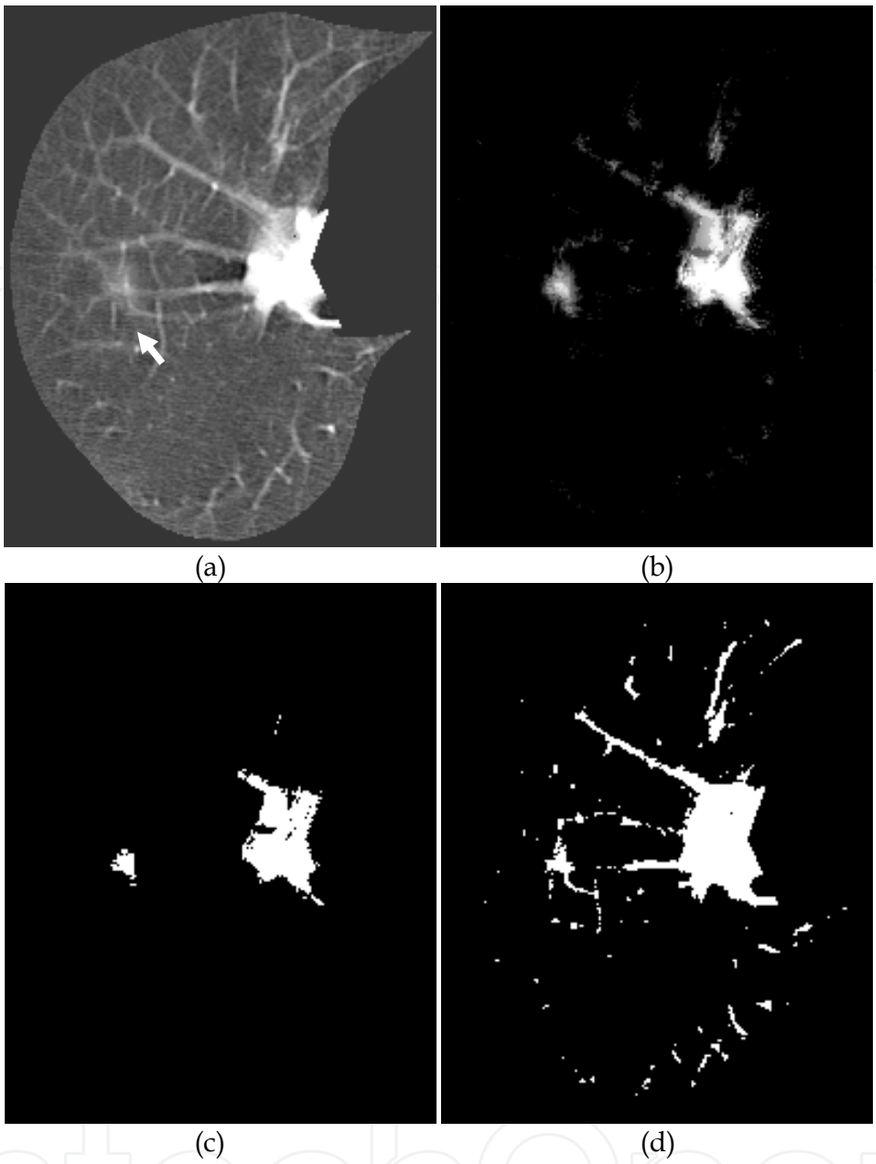

Fig. 6. Enhancement of a lesion by the trained lesion-enhancement MTANN filter for a non-training case. (a) Original image of the segmented lung with a nodule (indicated by an arrow). (b) Output image of the trained lesion-enhancement MTANN filter. The nodule is enhanced in the output image, whereas most of the normal structures are suppressed. (c) Nodule candidates detected by the trained lesion-enhancement MTANN followed by thresholding. (d) Nodule candidates detected by simple thresholding only.

4.4. Classification of Nodule Candidates

Nodule candidates generally include true positives and mostly FPs. For reduction of the FPs, we trained an MTANN for classification of nodule candidates into nodules or non-nodules (Suzuki, Armato et al. 2003; Suzuki, Yoshida et al. 2008). We used 10 different-sized nodules with various contrasts and 10 non-nodule images including medium-sized and small vessels as training cases for the MTANN, as shown in Fig. 7. Parameters such as the

size of the subregion of the MTANN, the standard deviation of the 2D Gaussian function in the teaching image, and the size of the teaching image were determined by experimental analysis (16) to be 9 x 9 pixels, 5.0 pixels, and 19 x 19 pixels, respectively. We employed a three-layer structure for the MTANN, because it has been proved theoretically that a three-layer ANN can approximate any continuous mapping (38,39). The number of hidden units in the MTANN was determined to be 20 by use of a method for determining the structure of an ANN (40,41). Thus, the numbers of input, hidden, and output units were 81, 20, and one, respectively. With the parameters above, the training of the MTANN was performed 500,000 times, and it converged with a mean absolute error of 0.112. Figure 7 shows the input images used for training the MTANN and the output images of the trained MTANN. It is apparent that the nodules are represented by light "fuzzy nodular" distributions in the output images, whereas the vessels are dark and thus "almost removed."

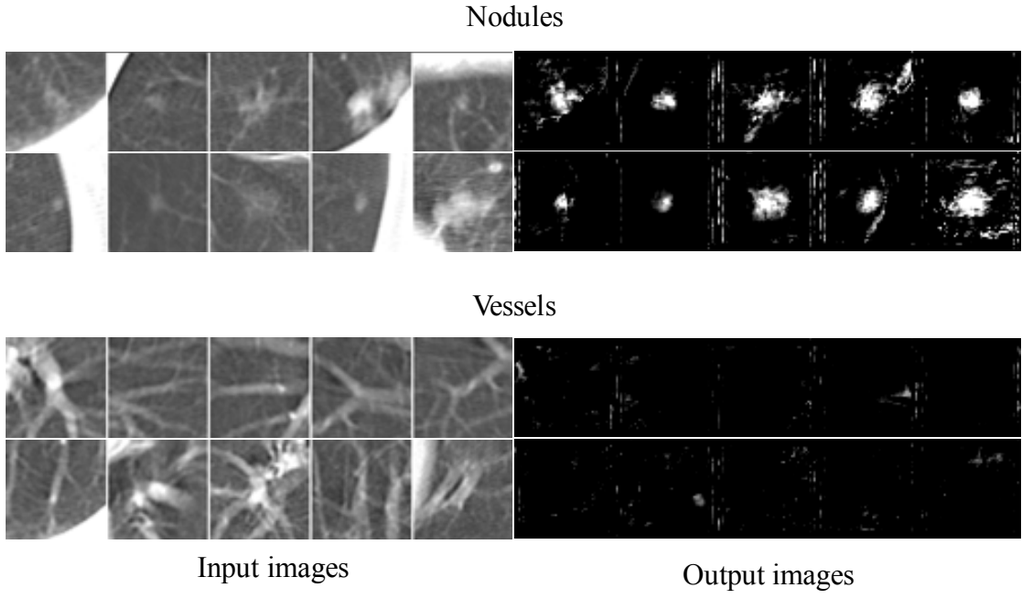

Fig. 7. Ten nodules and 10 non-nodule images including vessels used for training an MTANN, and the corresponding output images of the trained MTANN. The nodules are various-sized with different contrasts. The non-nodule images include medium-sized and small vessels with various orientations, which are the majority of non-nodules in the lungs.

4.5. Simulated CT Images

To investigate the basic characteristics of the trained MTANNs, we created simulated CT images that contained model nodules and model vessels. A nodule was modeled as a sphere, and a vessel as a cylinder. The simulated images included various-sized model nodules (8.0 mm, 14.0 mm, and 20.0 mm in diameter) with low, medium, and high contrast [200 Hounsfield units (HU), 400 HU, and 600 HU], various-sized model vessels (2.0 mm, 3.0 mm, and 4.0 mm in diameter) with different orientations such as horizontal, vertical, and diagonal, and model nodules overlapping with model vessels, as shown in Fig. 8(a). We created the same-sized model nodules with different contrasts, because solid opacity and

ground-glass opacity (GGO) of the same size have different contrasts. The background level was -900 HU, which corresponds to the average background level in the lungs.
Figure 8(b) shows the output image of the MTANN trained with actual nodules. In the output image, the various-sized model nodules with different contrasts are represented by light "nodular" distributions, whereas various-sized model vessels with different orientations are almost dark, and are thus removed. Therefore, it is apparent in the figure that model nodules can be distinguished from model vessels. This result indicates that the MTANN was able to learn from a very small number of training actual cases (10 actual nodules and 10 actual vessel images) to enhance sphere-like objects (model nodules) and suppress cylinder-like objects (model vessels), and that the trained MTANN would be robust against a change in scale and rotation.

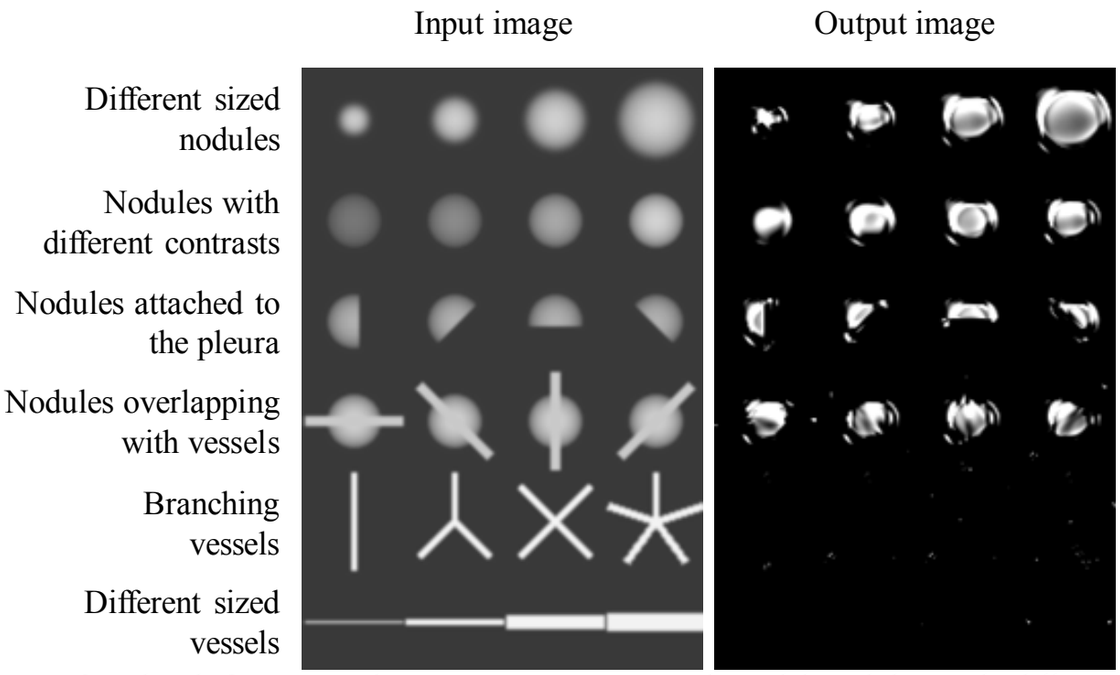

Fig. 8. Simulated CT image that contains various-sized model nodules with different contrasts and various-sized model vessels with different orientations, and the corresponding output images of the MTANNs trained with 10 actual nodules and 10 actula vessel images. (a) Input image for the MTANNs. (b) Output image of the trained MTANN.

4.6. Performance of a CAD Scheme

In order to investigate the performance for actual nodules and vessels, we applied the trained MTANN to non-training cases. Figures 9(a) and (b) show the output images of the trained MTANN, where various-sized actual nodules with different contrasts are represented by light "nodular" distributions, whereas medium-sized and small actual vessels with different orientations are almost eliminated. To distinguish nodules from various types of non-nodules, we trained 6 classification-MTANNs with 10 typical nodules and 6 different types of 10 non-nodules such as medium-sized vessels, small vessels, large vessels, soft-tissue opacity, and abnormal opacities from a training database. We applied the

trained classification-MTANNs to various types of nodules and non-nodules. The trained classification-MTANNs enhance nodules and suppress most of normal structures including various-sized lung vessels in CT images, as shown in Fig. 9. The scores indicating the likelihood of being a nodule from the 6 classification-MTANNs were combined with a mixing ANN to form a mixture of expert classification-MTANNs. We used a leave-one-out cross-validation test for testing the mixing ANN in the mixture of expert MTANNs. We evaluated the performance by using free-response receiver-operating-characteristic (FROC) analysis (Egan, Greenberg et al. 1961).

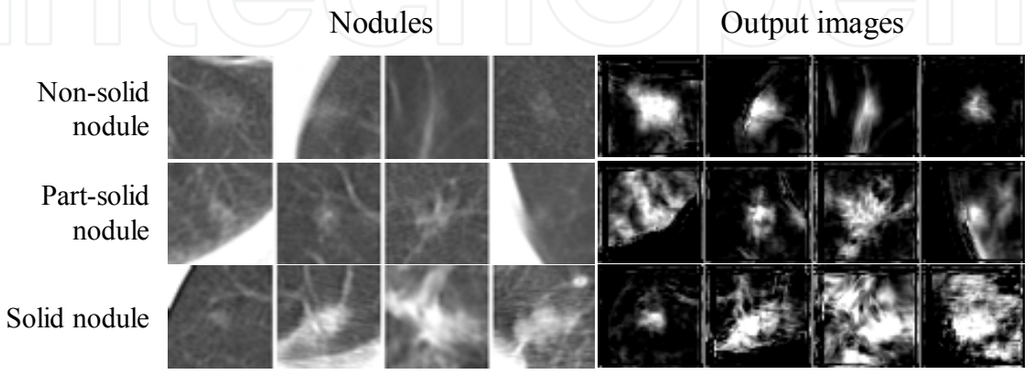

(a)

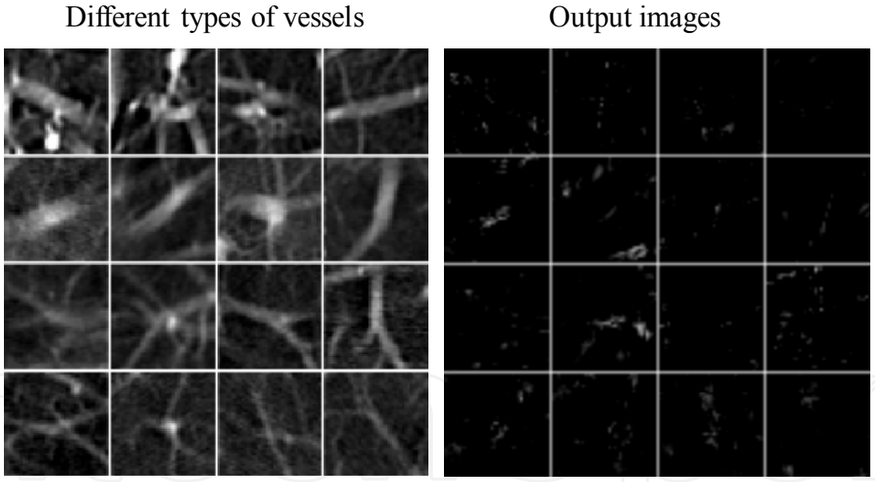

(b)

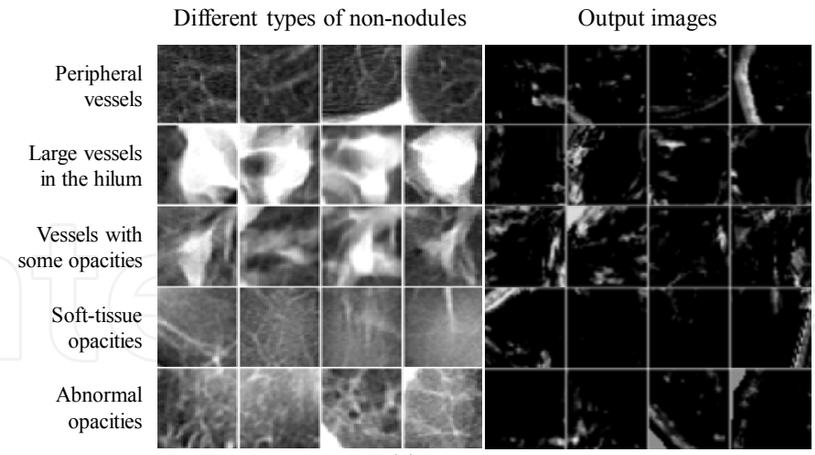

(c)

Fig. 9. Illustrations of (a) various types of actual nodules and the corresponding output images of the trained MTANN for non-training cases, (b) various-sized lung vessels and and the corresponding output images, and (c) other types of non-nodules and the corresponding output images.

To test the performance of our CAD scheme utilizing the MTANN lesion enhancement filter and the classification MTANNs, we applied it to the test database containing 69 lung cancers. The MTANN lesion enhancement filter followed by thresholding identified 97% (67/69) of cancers with 6.7 FPs per section. The classification-MTANNs were applied to the nodule candidates (true positives and FPs) for classification of the candidates into nodules or non-nodules. The scores from the 6 classification-MTANNs are shown in Fig. 10. Although the distributions for nodules and non-nodules overlap, many nodules can be separated from non-nodules by decision boundaries. The FROC curve indicating the performance of the mixture of expert MTANNs is shown in Fig. 11. The mixture of expert MTANNs was able to remove 60% (8,172/13,688) or 93% (12,667/13,688) of non-nodules (FPs) with a loss of 1 true positive or 10 true positives, respectively. Thus, our MTANN-based CAD scheme achieved a 96% (66/69) or 84% (57/69) sensitivity with 2.7 (5,516/2,052) or 0.5 (1,021/2,052) FPs per section. The remaining true-positive nodules included a ground-glass opacity, a cancer overlapping vessels, and a cancer touching the pleura. In contrast, the difference-image technique followed by multiple thresholding in the previously reported CAD scheme (Arimura, Katsuragawa et al. 2004) detected 96% (66/69) of cancers with 19.3 FPs per section. Thus, the MTANN lesion-enhancement filter was effective for improving the sensitivity and specificity of a CAD scheme. The feature analysis and the rule-based scheme removed FPs further and achieved 9.3 FPs per section. Finally, with LDA, the previously reported CAD scheme yielded a sensitivity of 84% (57/69) with 1.4 (2,873/2,052) FPs per section. Therefore, MTANNs were effective for improving the sensitivity and specificity of a CAD scheme.

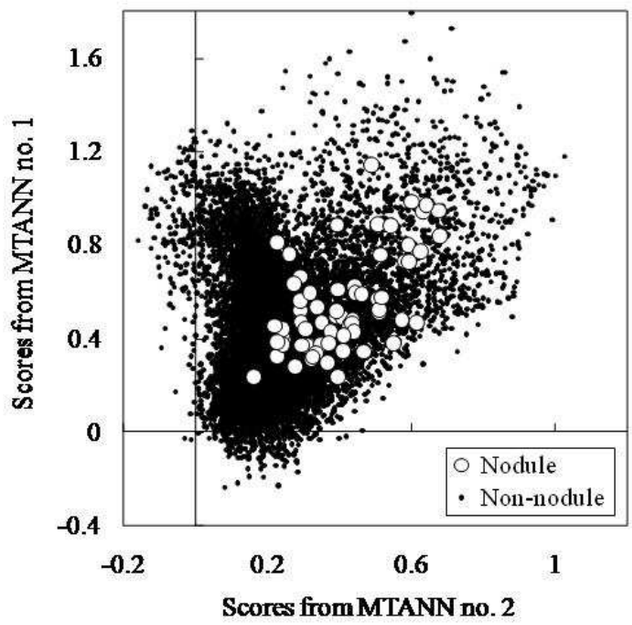

Fig. 10. Distributions of scores from MTANN nos. 1 and 2 of the 6 classification-MTANNs for 67 nodules (white circles) and 13,688 non-nodules (black dots) detected by the lesion-enhancement MTANN filter followed by thresholding.

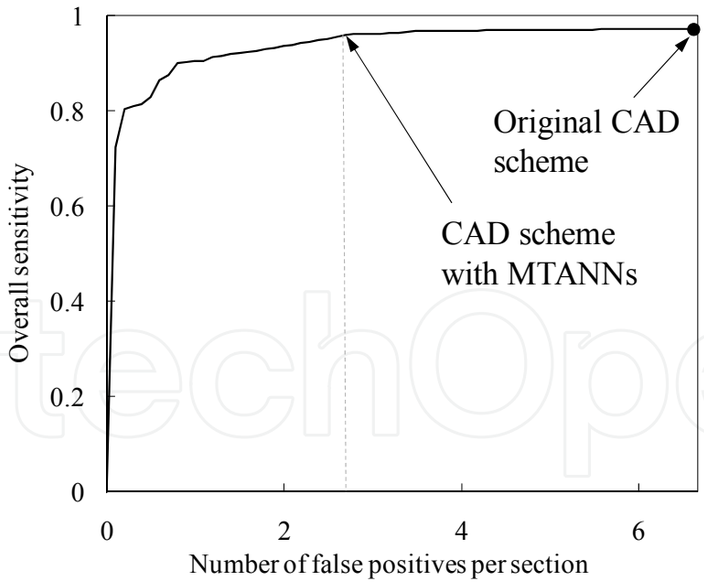

Fig. 11. Performance of the mixture of expert MTANNs for classification between 67 nodules and 13,688 non-nodules. The FROC curve indicates that the mixture of expert MTANNs yielded a reduction of 60% (8,172/13,688) or 93% (12,667/13,688) of non-nodules (FPs) with a loss of 1 true positive or 10 true positives, respectively, i.e., it achieved a 96% (66/69) or 84% (57/69) sensitivity with 2.7 (5,516/2,052) or 0.5 (1,021/2,052) FPs per section, respectively.

5. A CAD Scheme for Detection of Polyps in CTC

5.1. Colorectal Cancer Detection in CTC

Colorectal cancer is the second leading cause of cancer deaths in the United States (Jemal, Murray et al. 2005). Evidence suggests that early detection and removal of polyps (i.e., precursors of colorectal cancer) can reduce the incidence of colorectal cancer (Winawer, Fletcher et al. 1997; Dachman 2003). CT colonography (CTC), also known as virtual colonoscopy, is a technique for detecting colorectal neoplasms by use of a CT scan of the colon (Macari and Bini 2005). The diagnostic performance of CTC in detecting polyps, however, remains uncertain due to a propensity for perceptual errors (Fletcher, Booya et al. 2005). Computer-aided detection (CAD) of polyps has been investigated to overcome the difficulty with CTC. CAD has the potential to improve radiologists' diagnostic performance in the detection of polyps.

Although CAD schemes are useful for improving radiologists' sensitivity in detection of polyps in CTC, a major challenge for CAD schemes is reducing the number of FPs, while maintaining high sensitivity. Major sources of FPs generated by CAD schemes include haustral folds, residual stool, rectal tubes, the ileocecal valve, and extra-colonic structures such as the small bowel and stomach (Yoshida and Dachman 2005). Among those FP sources, rectal tubes are relatively obvious FPs. Radiologists may, however, lose their confidence in CAD as an effective tool if the CAD scheme generates such obvious FPs. Therefore, removal of rectal-tube-induced FPs is desirable. To address this issue, we previously reported a 3D MTANN for distinction between polyps and rectal tubes in 3D CTC volumetric data (Suzuki, Yoshida et al. 2006). The 3D MTANN eliminated all rectal-tube-induced FPs without removal of any true positives. Our purpose in this study was to develop a "mixture of expert" 3D MTANNs for further reduction of FPs in a polyp-detection CAD scheme while maintaining high sensitivity.

5.2. CTC Database

CTC examinations were performed on 73 patients at The University of Chicago Medical Center. The patients' colons were prepared by standard pre-colonoscopy cleansing with administration of cathartics following a water diet or low-fiber diet, and they were insufflated with room air or carbon dioxide. Each patient was scanned in both supine and prone positions. Our database thus contained 146 CTC datasets. The CT scans were performed with either a single- or a multi-detector-row CT scanner (HiSpeed CTi or LightSpeed QX/i, GE Medical Systems, Milwaukee, WI). The CT scanning parameters included collimations between 2.5 and 5.0 mm, reconstruction intervals of 1.0-5.0 mm [1.0 mm (n=2, 1% of the CTC datasets), 1.25 mm (n=3, 2%), 1.5 mm (n=59, 41%), 2.5 mm (n=79, 54%), and 5.0 mm (n=3, 2%)], and tube currents of 60-120 mA with 120 kVp. Each reconstructed CT section had a matrix size of 512 x 512 pixels, with an in-plane pixel size of 0.5-0.7 mm. The CT sections were interpolated to isotropic resolution by use of linear interpolation in the transverse direction. All patients underwent "reference-standard" optical colonoscopy. Radiologists established the locations of polyps in the CTC datasets by use of the colonoscopy and pathology reports, as well as multiplanar reformatted views of the CTC on a viewing workstation (GE Advantage Windows Workstation v.4.2, GE Medical Systems, Milwaukee, WI). In this study, we used 5 mm as the threshold for clinically significant polyps(Johnson and Dachman 2000). Fifteen patients had 28 polyps, 15 of which

were 5-9 mm in diameter, and 13 were 10-25 mm. There was no polyp that was submerged in fluid. Fluid was minimized by use of a saline cathartic preparation as the standard preparation, not a colon gavage. We also created a training database of non-polyps by manual extraction of volumes containing non-polyps from 27 "normal" (non-polyp) CTC cases.

5.3. Performance of Our Initial CAD Scheme

We applied our previously reported CAD scheme (Yoshida and Nappi 2001; Nappi and Yoshida 2003) to the 73 CTC cases. The scheme included centerline-based extraction of the colon (Frimmel, Nappi et al. 2004), shape-based detection of polyps (Yoshida and Näppi 2001; Yoshida, Masutani et al. 2002), and initial reduction of FPs by use of a Bayesian ANN (Kupinski, Edwards et al. 2001) based on geometric and texture features (Nappi and Yoshida 2002; Nappi and Yoshida 2003). We evaluated supine and prone CTC volumes independently. This CAD scheme achieved a 96.4% (27/28 polyps) by-polyp sensitivity with an average of 3.1 (224/73) FPs per patient. Forty-eight true-positive polyp detections in both supine and prone CTC volumes represented 27 polyps. We combined our previously reported CAD scheme with the mixture of expert 3D MTANNs for further reduction of FPs.

5.4. Training of Expert 3D MTANNs

We manually selected ten representative polyp volumes (ten polyps) from the 48 true-positive volumes (containing 27 polyps) in our CTC database as the training polyp cases for expert 3D MTANNs. We classified CAD-generated FP sources into eight categories, i.e., rectal tubes, small bulbous folds, solid stool, stool with bubbles, colonic walls with haustral folds, elongated folds, strip-shaped folds, and the ileocecal valve. We manually selected ten non-polyps in each of the eight categories from the training non-polyp database (which was not used for testing). The ten polyps and the ten rectal tubes were the same as those used in our previous study (Suzuki, Yoshida et al. 2006). The number of sample volumes for each category was ten, because the performance of an expert 3D MTANN was found to be highest when the number of training sample volumes was 20 (i.e., ten polyps and ten non-polyps) in our previous study (Suzuki, Yoshida et al. 2006), and the performance of 2D/3D MTANNs was not sensitive to the number of sample regions/volumes over different types of non-lesions in our previous studies (Suzuki, Armato et al. 2003; Suzuki, Armato et al. 2003; Suzuki and Doi 2005; Suzuki, Li et al. 2005; Suzuki, Yoshida et al. 2006).

We trained eight expert 3D MTANNs with the ten polyps and ten non-polyps in each category. A three-layer structure was employed for the expert 3D MTANNs(Funahashi 1989). The size of the training volume and the standard deviation of the 3D Gaussian distribution in the teaching volume were 15 x 15 x 15 voxels (i.e., cubic shape) and 4.5 voxels, respectively, which were determined empirically based on our previous studies (Suzuki, Armato et al. 2003; Arimura, Katsuragawa et al. 2004; Suzuki and Doi 2005; Suzuki, Yoshida et al. 2006). The number of hidden units was selected to be 25 by use of a method for designing the structure of an ANN (Suzuki, Horiba et al. 2001; Suzuki 2004). With the parameters above, training of the expert 3D MTANNs was performed by 500,000 iterations. We selected four among the eight expert 3D MTANNs for the mixture of expert 3D MTANNs by experimental analysis, because the mixture of these four expert 3D MTANNs

((1) rectal tubes, (2) stool with bubbles, (3) colonic walls with haustral folds, and (4) solid stool) demonstrated the highest performance (described in the next subsection).

5.5. Evaluation of the Performance for False-Positive Reduction

We applied the trained expert 3D MTANNs to the 27 polyps (48 true-positive volumes) and all 224 non-training FPs identified by our previously reported CAD scheme. The output volumes for these testing cases are shown in Fig. 12. The centers of the input volumes corresponded to the detection results provided by the CAD scheme (including both true positives and FPs); thus, this experiment included the effect of actual off-centering of polyp candidates produced by the initial CAD scheme. Various polyps, including a sessile polyp (the third image from the left in Fig. 12(a)), are represented in the output by distributions of bright voxels, whereas various types of non-polyps appear as darker voxels, indicating the ability of the expert 3D MTANNs to enhance polyps and suppress different types of non-polyps. We applied the 3D scoring method to the output volumes for polyps and non-polyps. The 3D Gaussian weighting function used the same standard deviation as that for the 3D Gaussian distribution in the polyp teaching volume. Distributions of scores from the expert 3D MTANNs for the 27 polyps and all FPs are shown in Fig. 13. Although the two distributions in each graph overlap, a substantial fraction of FPs can be eliminated by use of the expert 3D MTANNs.

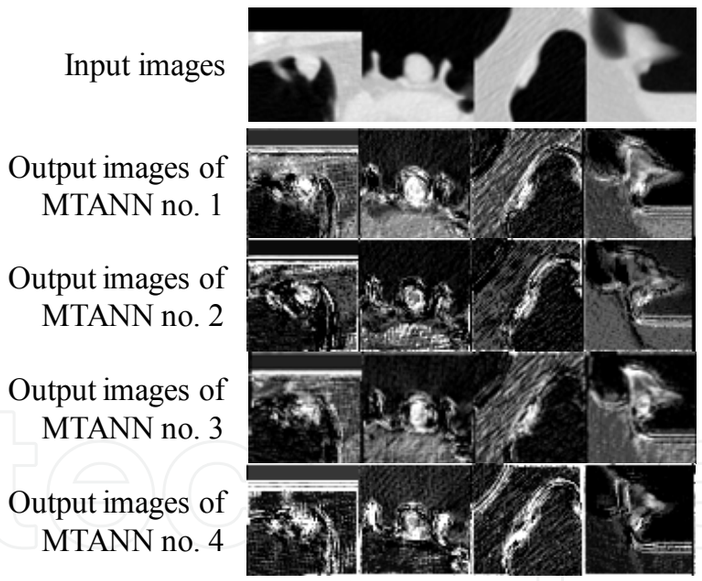

(a)

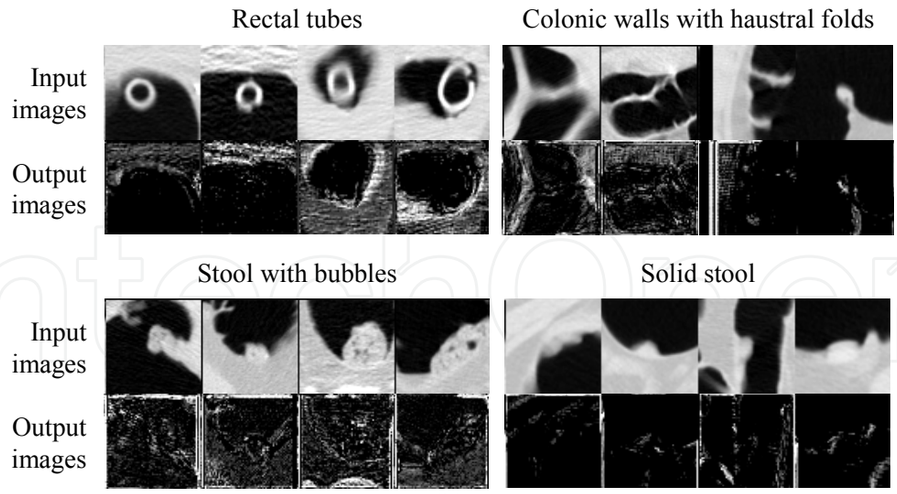

(b)

Fig. 12. Illustrations of (a) various testing polyps and the corresponding output volumes of four trained expert 3D MTANNs and (b) four different categories of testing FPs and the output volumes from corresponding expert 3D MTANNs. In the output volumes, polyps appear as distributions of bright voxels (i.e., they are enhanced), whereas different types of FPs appear as dark voxels (i.e., they are suppressed).

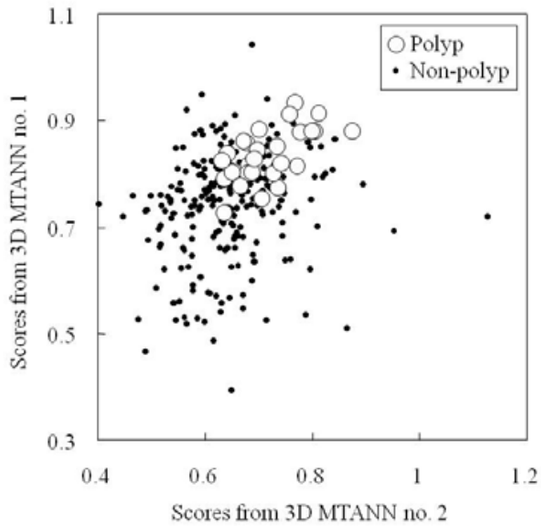

Fig. 13. Distributions of scores from MTANN nos. 1 and 2 in the mixture of expert 3D MTANNs for 27 polyps (white circles) and 224 non-polyps (black dots).

We evaluated the overall performance of the mixture of expert 3D MTANNs for FP reduction by use of free-response receiver-operating-characteristic (FROC) analysis (Egan, Greenberg et al. 1961). The FROC curve of the trained mixture of expert 3D MTANNs is shown in Fig. 14. The FROC curve was obtained by a change in the threshold value for the output of the mixing ANN. This FROC curve indicates that the mixture of expert 3D MTANNs was able to eliminate 63% (142/224) of non-polyps (FPs) without removal of any

of the 27 polyps, i.e., a 96.4% (27/28) overall by-polyp sensitivity was achieved at an FP rate of 1.1 (82/73) per patient.

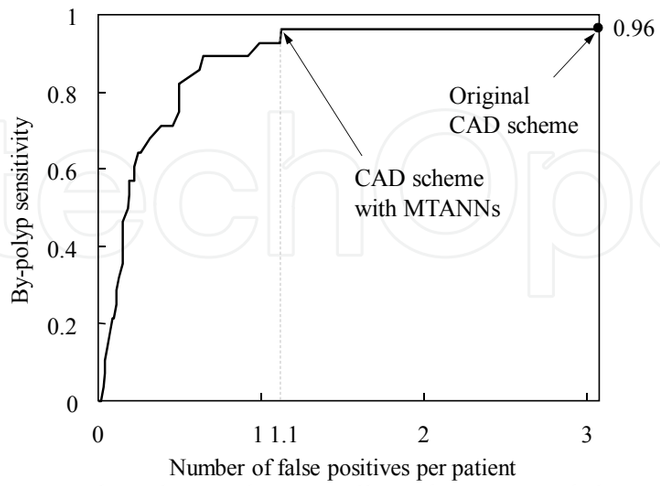

Fig. 14. The FROC curve that shows the overall performance of the mixture of expert 3D MTANNs when it was applied to the entire database of 27 polyps (48 true-positive volumes) and 224 FPs. The FROC curve indicates that the mixture of expert 3D MTANNs yielded a reduction of 63% (142/224) of non-polyps (FPs) without removal of any true positives, i.e., it achieved 100% (27/27 or 17/17) classification performance.

6. Conclusion

The MTANN supervised filter was effective for enhancement of lesions including lung nodules and colorectal polyps and suppression of non-lesions in medical images and was useful for improving the sensitivity and specificity of CAD schemes substantially.

7. References

American:Cancer:Society (2005). Cancer Facts and Figures 2005. Atlanta, American Cancer Society.

Arimura, H., S. Katsuragawa, et al. (2004). "Computerized scheme for automated detection of lung nodules in low-dose computed tomography images for lung cancer screening." Academic Radiology 11(6): 617-629.

Armato, S. G., 3rd, M. L. Giger, et al. (2001). "Automated detection of lung nodules in CT scans: preliminary results." Medical Physics 28(8): 1552-1561.

Armato, S. G., 3rd, M. L. Giger, et al. (1999). "Computerized detection of pulmonary nodules on CT scans." Radiographics 19(5): 1303-1311.

Armato, S. G., 3rd, F. Li, et al. (2002). "Lung cancer: performance of automated lung nodule detection applied to cancers missed in a CT screening program." Radiology 225(3): 685-692.

Chan, H. P., K. Doi, et al. (1987). "Image feature analysis and computer-aided diagnosis in digital radiography. I. Automated detection of microcalcifications in mammography." Medical Physics 14(4): 538-548.

Dachman, A. H. (2003). Atlas of Virtual Colonoscopy. New York, Springer-Verlag.

Dean, J. C. and C. C. Ilvento (2006). "Improved cancer detection using computer-aided detection with diagnostic and screening mammography: prospective study of 104 cancers." AJR Am J Roentgenol 187(1): 20-8.

Drukker, K., M. L. Giger, et al. (2005). "Robustness of computerized lesion detection and classification scheme across different breast US platforms." Radiology 237(3): 834-40.

Egan, J. P., G. Z. Greenberg, et al. (1961). "Operating characteristics, signal detectability, and the method of free response." Journal of the Acoustical Society of America 33: 993-1007.

Flehinger, B. J., M. Kimmel, et al. (1992). "The effect of surgical treatment on survival from early lung cancer. Implications for screening." Chest 101(4): 1013-1018.

Flehinger, B. J., M. R. Melamed, et al. (1984). "Early lung cancer detection: results of the initial (prevalence) radiologic and cytologic screening in the Memorial Sloan-Kettering study." American Review of Respiratory Disease 130(4): 555-560.

Fletcher, J. G., F. Booya, et al. (2005). "CT colonography: unraveling the twists and turns." Curr Opin Gastroenterol 21(1): 90-8.

Fontana, R. S., D. R. Sanderson, et al. (1984). "Early lung cancer detection: results of the initial (prevalence) radiologic and cytologic screening in the Mayo Clinic study." American Review of Respiratory Disease 130(4): 561-565.

Frangi, A. F., W. J. Niessen, et al. (1999). "Model-based quantitation of 3-D magnetic resonance angiographic images." IEEE Trans Med Imaging 18(10): 946-56.

Frimmel, H., J. Nappi, et al. (2004). "Fast and robust computation of colon centerline in CT colonography." Medical Physics 31(11): 3046-3056.

Frost, J. K., W. C. Ball, Jr., et al. (1984). "Early lung cancer detection: results of the initial (prevalence) radiologic and cytologic screening in the Johns Hopkins study." American Review of Respiratory Disease 130(4): 549-554.

Funahashi, K. (1989). "On the approximate realization of continuous mappings by neural networks." Neural Networks 2: 183-192.

Giger, M. L., K. Doi, et al. (1988). "Image feature analysis and computer-aided diagnosis in digital radiography. 3. Automated detection of nodules in peripheral lung fields." Medical Physics 15(2): 158-166.

Giger, M. L. and K. Suzuki (2007). Computer-Aided Diagnosis (CAD). Biomedical Information Technology. D. D. Feng, Academic Press: 359-374.

Gilhuijs, K. G., M. L. Giger, et al. (1998). "Computerized analysis of breast lesions in three dimensions using dynamic magnetic-resonance imaging." Med Phys 25(9): 1647-54.

Gurney, J. W. (1996). "Missed lung cancer at CT: imaging findings in nine patients." Radiology 199(1): 117-122.

Heelan, R. T., B. J. Flehinger, et al. (1984). "Non-small-cell lung cancer: results of the New York screening program." Radiology 151(2): 289-293.

Henschke, C. I., D. I. McCauley, et al. (1999). "Early Lung Cancer Action Project: overall design and findings from baseline screening." Lancet 354(9173): 99-105.

Henschke, C. I., D. P. Naidich, et al. (2001). "Early lung cancer action project: initial findings on repeat screenings." Cancer 92(1): 153-159.

Horsch, K., M. L. Giger, et al. (2004). "Performance of computer-aided diagnosis in the interpretation of lesions on breast sonography." Acad Radiol 11(3): 272-80.

Jemal, A., T. Murray, et al. (2005). "Cancer statistics, 2005." CA Cancer J Clin 55(1): 10-30.
Jemal, A., T. Murray, et al. (2005). "Cancer statistics, 2005." CA: A Cancer Journal for Clinicians 55(1): 10-30.
Johnson, C. D. and A. H. Dachman (2000). "CT colonography: the next colon screening examination?" Radiology 216(2): 331-341.
Kaneko, M., K. Eguchi, et al. (1996). "Peripheral lung cancer: screening and detection with low-dose spiral CT versus radiography." Radiology 201(3): 798-802.
Kobayashi, T., X. W. Xu, et al. (1996). "Effect of a computer-aided diagnosis scheme on radiologists' performance in detection of lung nodules on radiographs." Radiology 199(3): 843-848.
Kubik, A. and J. Polak (1986). "Lung cancer detection. Results of a randomized prospective study in Czechoslovakia." Cancer 57(12): 2427-2437.
Kupinski, M. A., D. C. Edwards, et al. (2001). "Ideal observer approximation using Bayesian classification neural networks." IEEE Trans Med Imaging 20(9): 886-99.
Li, F., M. Aoyama, et al. (2004). "Radiologists' performance for differentiating benign from malignant lung nodules on high-resolution CT using computer-estimated likelihood of malignancy." AJR. American Journal of Roentgenology 183(5): 1209-1215.
Li, F., H. Arimura, et al. (2005). "Computer-aided detection of peripheral lung cancers missed at CT: ROC analyses without and with localization." Radiology 237(2): 684-90.
Li, F., S. Sone, et al. (2002). "Lung cancers missed at low-dose helical CT screening in a general population: comparison of clinical, histopathologic, and imaging findings." Radiology 225(3): 673-683.
Macari, M. and E. J. Bini (2005). "CT colonography: where have we been and where are we going?" Radiology 237(3): 819-33.
Miettinen, O. S. (2000). "Screening for lung cancer." Radiologic Clinics of North America 38(3): 479-486.
Miettinen, O. S. and C. I. Henschke (2001). "CT screening for lung cancer: coping with nihilistic recommendations." Radiology 221(3): 592-596.
Mosier, C. I. (1951). "Problems and designs of cross-validation." Educational and Psychological Measurement 11: 5-11.
Nappi, J. and H. Yoshida (2002). "Automated detection of polyps with CT colonography: evaluation of volumetric features for reduction of false-positive findings." Academic Radiology 9(4): 386-397.
Nappi, J. and H. Yoshida (2003). "Feature-guided analysis for reduction of false positives in CAD of polyps for computed tomographic colonography." Medical Physics 30(7): 1592-1601.
Nawa, T., T. Nakagawa, et al. (2002). "Lung cancer screening using low-dose spiral CT: results of baseline and 1-year follow-up studies." Chest 122(1): 15-20.
Oja, E. (1983). Subspace methods of pattern recognition. Letchworth, Hertfordshire, England; New York, Research Studies Press; Wiley.
Otsu, N. (1979). "A Threshold Selection Method from Gray Level Histograms." IEEE Transactions on Systems, Man and Cybernetics 9(1): 62-66.
Rumelhart, D. E., G. E. Hinton, et al. (1986). "Learning representations by back-propagating errors." Nature 323: 533-536.

Sobue, T., T. Suzuki, et al. (1992). "Survival for clinical stage I lung cancer not surgically treated. Comparison between screen-detected and symptom-detected cases. The Japanese Lung Cancer Screening Research Group." Cancer 69(3): 685-692.

Sone, S., F. Li, et al. (2001). "Results of three-year mass screening programme for lung cancer using mobile low-dose spiral computed tomography scanner." British Journal of Cancer 84(1): 25-32.

Sone, S., S. Takashima, et al. (1998). "Mass screening for lung cancer with mobile spiral computed tomography scanner." Lancet 351(9111): 1242-1245.

Suzuki, K. (2004). "Determining the receptive field of a neural filter." Journal of Neural Engineering 1(4): 228-237.

Suzuki, K., H. Abe, et al. (2006). "Image-processing technique for suppressing ribs in chest radiographs by means of massive training artificial neural network (MTANN)." IEEE Transactions on Medical Imaging 25(4): 406-416.

Suzuki, K., S. G. Armato, et al. (2003). Effect of a small number of training cases on the performance of massive training artificial neural network (MTANN) for reduction of false positives in computerized detection of lung nodules in low-dose CT. Proc. SPIE Medical Imaging (SPIE MI), San Diego, CA.

Suzuki, K., S. G. Armato, et al. (2003). "Massive training artificial neural network (MTANN) for reduction of false positives in computerized detection of lung nodules in low-dose CT." Medical Physics 30(7): 1602-1617.

Suzuki, K. and K. Doi (2005). "How can a massive training artificial neural network (MTANN) be trained with a small number of cases in the distinction between nodules and vessels in thoracic CT?" Academic Radiology 12(10): 1333-1341.

Suzuki, K., I. Horiba, et al. (2001). "A simple neural network pruning algorithm with application to filter synthesis." Neural Processing Letters 13(1): 43-53.

Suzuki, K., I. Horiba, et al. (2002). "Efficient approximation of neural filters for removing quantum noise from images." IEEE Transactions on Signal Processing 50(7): 1787-1799.

Suzuki, K., I. Horiba, et al. (2003). "Neural edge enhancer for supervised edge enhancement from noisy images." IEEE Transactions on Pattern Analysis and Machine Intelligence 25(12): 1582-1596.

Suzuki, K., I. Horiba, et al. (2004). "Extraction of left ventricular contours from left ventriculograms by means of a neural edge detector." IEEE Transactions on Medical Imaging 23(3): 330-339.

Suzuki, K., F. Li, et al. (2005). "Computer-aided diagnostic scheme for distinction between benign and malignant nodules in thoracic low-dose CT by use of massive training artificial neural network." IEEE Transactions on Medical Imaging 24(9): 1138-1150.

Suzuki, K., J. Shiraishi, et al. (2005). "False-positive reduction in computer-aided diagnostic scheme for detecting nodules in chest radiographs by means of massive training artificial neural network." Academic Radiology 12(2): 191-201.

Suzuki, K., H. Yoshida, et al. (2008). "Mixture of expert 3D massive-training ANNs for reduction of multiple types of false positives in CAD for detection of polyps in CT colonography." Med Phys 35(2): 694-703.

Suzuki, K., H. Yoshida, et al. (2006). "Massive-training artificial neural network (MTANN) for reduction of false positives in computer-aided detection of polyps: Suppression of rectal tubes." Medical Physics 33(10): 3814-3824.

Swensen, S. J., J. R. Jett, et al. (2003). "Lung cancer screening with CT: Mayo Clinic experience." Radiology 226(3): 756-761.

van Ginneken, B., B. M. ter Haar Romeny, et al. (2001). "Computer-aided diagnosis in chest radiography: a survey." IEEE Transactions on Medical Imaging 20(12): 1228-1241.

Winawer, S. J., R. H. Fletcher, et al. (1997). "Colorectal cancer screening: clinical guidelines and rationale." Gastroenterology 112(2): 594-642.

Yoshida, H. and A. H. Dachman (2005). "CAD techniques, challenges, and controversies in computed tomographic colonography." Abdom Imaging 30(1): 26-41.

Yoshida, H., Y. Masutani, et al. (2002). "Computerized detection of colonic polyps at CT colonography on the basis of volumetric features: pilot study." Radiology 222(2): 327-36.

Yoshida, H. and J. Nappi (2001). "Three-dimensional computer-aided diagnosis scheme for detection of colonic polyps." IEEE Trans Med Imaging 20(12): 1261-74.

Yoshida, H. and J. Näppi (2001). "Three-dimensional computer-aided diagnosis scheme for detection of colonic polyps." IEEE Trans Med Imaging 20(12): 1261-74.

Machine Learning

Edited by Yagang Zhang

ISBN 978-953-307-033-9
Hard cover, 438 pages
Publisher InTech
Published online 01, February, 2010
Published in print edition February, 2010

Machine learning techniques have the potential of alleviating the complexity of knowledge acquisition. This book presents today's state and development tendencies of machine learning. It is a multi-author book. Taking into account the large amount of knowledge about machine learning and practice presented in the book, it is divided into three major parts: Introduction, Machine Learning Theory and Applications. Part I focuses on the introduction to machine learning. The author also attempts to promote a new design of thinking machines and development philosophy. Considering the growing complexity and serious difficulties of information processing in machine learning, in Part II of the book, the theoretical foundations of machine learning are considered, and they mainly include self-organizing maps (SOMs), clustering, artificial neural networks, nonlinear control, fuzzy system and knowledge-based system (KBS). Part III contains selected applications of various machine learning approaches, from flight delays, network intrusion, immune system, ship design to CT and RNA target prediction. The book will be of interest to industrial engineers and scientists as well as academics who wish to pursue machine learning. The book is intended for both graduate and postgraduate students in fields such as computer science, cybernetics, system sciences, engineering, statistics, and social sciences, and as a reference for software professionals and practitioners.

How to reference

In order to correctly reference this scholarly work, feel free to copy and paste the following:

Kenji Suzuki Ph.D. (2010). Massive-Training Artificial Neural Networks (MTANN) in Computer-Aided Detection of Colorectal Polyps and Lung Nodules in CT, Machine Learning, Yagang Zhang (Ed.), ISBN: 978-953-307-033-9, InTech, Available from: http://www.intechopen.com/books/machine-learning/massive-training-artificial-neural-networks-mtann-in-computer-aided-detection-of-colorectal-polyps-a

INTECH
open science | open minds

InTech Europe
University Campus STeP Ri
Slavka Krautzeka 83/A
51000 Rijeka, Croatia
Phone: +385 (51) 770 447
Fax: +385 (51) 686 166
www.intechopen.com

InTech China
Unit 405, Office Block, Hotel Equatorial Shanghai
No.65, Yan An Road (West), Shanghai, 200040, China
中国上海市延安西路65号上海国际贵都大饭店办公楼405单元
Phone: +86-21-62489820
Fax: +86-21-62489821

IntechOpen